



Estimate hourly PM_{2.5} concentrations from Himawari-8 TOA reflectance directly using geo-intelligent long short-term memory network[☆]

Bin Wang^a, Qiangqiang Yuan^{a,*}, Qianqian Yang^a, Liye Zhu^b, Tongwen Li^c, Liangpei Zhang^d

^a School of Geodesy and Geomatics, Wuhan University, Wuhan, China

^b School of Atmospheric Sciences, Sun Yat-Sen University, Guangzhou, China

^c School of Geospatial Engineering and Science, Sun Yat-Sen University, Guangzhou, China

^d State Key Laboratory of Information Engineering in Surveying, Mapping and Remote Sensing, Wuhan University, Wuhan, China

ARTICLE INFO

Article history:

Received 12 September 2020

Received in revised form

7 December 2020

Accepted 15 December 2020

Available online 16 December 2020

Keywords:

LSTM

PM_{2.5} estimation

Himawari-8

TOA reflectance

Geospatial autocorrelation

Pollution event

ABSTRACT

Fine particulate matter (PM_{2.5}) has attracted extensive attention because of its baneful influence on human health and the environment. However, the sparse distribution of PM_{2.5} measuring stations limits its application to public utility and scientific research, which can be remedied by satellite observations. Therefore, we developed a Geo-intelligent long short-term network (Geoi-LSTM) to estimate hourly ground-level PM_{2.5} concentrations in 2017 in Wuhan Urban Agglomeration (WUA). We conducted contrast experiments to verify the effectiveness of our model and explored the optimal modeling strategy. It turned out that Geoi-LSTM with TOA reflectance, meteorological conditions, and NDVI as inputs performs best. The station-based cross-validation R², root mean squared error and mean absolute error are 0.82, 15.44 μg/m³, 10.63 μg/m³, respectively. Based on model results, we revealed spatiotemporal characteristics of PM_{2.5} in WUA. Generally speaking, during the day, PM_{2.5} concentration remained stable at a relatively high level in the morning and decreased continuously in the afternoon. While during the year, PM_{2.5} concentrations were highest in winter, lowest in summer, and in-between in spring and autumn. Combined with meteorological conditions, we further analyzed the whole process of a PM_{2.5} pollution event. Finally, we discussed the loss in removing clouds-covered pixels and compared our model with several popular models. Overall, our results can reflect hourly PM_{2.5} concentrations seamlessly and accurately with a spatial resolution of 5 km, which benefits PM_{2.5} exposure evaluations and policy regulations.

© 2020 Elsevier Ltd. All rights reserved.

1. Introduction

With the rise of industrialization and urbanization, China has been suffering a very serious air pollution problem in recent ten

years. Compared with other air pollutants, PM_{2.5} (i.e. particulate matters with aerodynamic equivalents smaller than 2.5 μm in diameter) poses a more significant threat to human health, especially the respiratory system, which have been explored by plenty of studies (Leonardi et al., 2000; Qiu et al., 2014; Raaschou-Nielsen et al., 2013). In addition to physical health, researches also confirmed the damage of PM_{2.5} to human mental health (Chen et al., 2018). Monitoring PM_{2.5} concentration is of great importance because it can help the government make policies to protect citizens' health and reduce air pollution. However, the sparse distribution limits the spatial representativeness of station measurements. In other words, stations cannot provide precise information for residents who are relatively far from the monitoring station. The sparse distribution of stations hindered more precise air pollution

Abbreviations: Geoi-LSTM, Geo-intelligent long short-term network; **WUA**, Wuhan Urban Agglomeration; **TOA**, Top of atmosphere; **CV**, Cross-validation; **AOD**, Aerosol optical depth; **CNEMC**, China National Environmental Monitoring Center; **HPEMCS**, Hubei Provincial Environmental Monitoring Center Station; **LT**, Local time; **MLR**, multiple linear regression; **GWR**, Geographically weighted regression; **LME**, Linear mixed effect model; **GRNN**, General regression neural networks; **RF**, Random forest.

[☆] This paper has been recommended for acceptance by Prof. Pavlos Kassomenos.

* Corresponding author.

E-mail address: qqyuan@sgg.whu.edu.cn (Q. Yuan).

researches as well. Therefore, satellite remote sensing technology, which can carry out spatially continuous observation, was adopted to compensate for the shortcomings of ground-level measurements.

Three mainstream methods were introduced to reflect the relationship between satellite observations and PM_{2.5} concentrations: chemical simulation models (Werner et al., 2019), semi-empirical models (Zeng et al., 2018), and statistical models (Tzanis et al., 2019). Among them, statistical methods have become the most popular way because they do not require prior knowledge (Liu, 2014). In earlier studies, the simple linear regression model and multiple linear regression model (MLR) were introduced to research the relationship between the aerosol optical depth (AOD), meteorological conditions, and particulate matter (Gupta and Christopher, 2009; Koelemeijer et al., 2006). A considerable number of researchers developed geographically weighted regression models (GWR) to reflect spatial heterogeneity (Hu et al., 2013; Yao et al., 2019). Lee et al. established a linear mixed effect model (LME) to reflect this relationship's temporal heterogeneity (Lee et al., 2011). However, it is difficult for traditional statistical models to capture the nonlinearity and spatiotemporal heterogeneity of the relationship between satellite observation and PM_{2.5} measurements affected by meteorological conditions (Li et al., 2017a). Machine learning methods showed great potential in complex relationship learning and were gradually introduced into the PM_{2.5} concentration studies (Belgiu and Drăguț, 2016; Yang et al., 2018). For example, random forest (RF) as a representative of ensemble learning was widely used in all kinds of meteorological researches (Huang et al., 2018; Stafoggia et al., 2019); General regression neural networks (GRNN) and other neural networks were also used to mapping ground-level PM_{2.5} (Li et al., 2020; Zang et al., 2018). Besides, several researchers have attempted using deep learning methods, which is considered the second generation of neural network and can excavate more complex nonlinear relations between variables, to predict or estimate PM_{2.5} concentration (Eslami et al., 2019; Li et al., 2017b).

Studies in early years mostly adopted data from polar-orbiting satellites (e.g., Terra and Aqua), so the temporal resolution of results was limited to daily, from which we cannot comprehend the more precise process of PM_{2.5} variation (Hu et al., 2014; Ma et al., 2014; Xie et al., 2015). Compared to polar-orbiting satellites, geostationary satellites can provide products for specific areas with an hourly or higher temporal resolution. Himawari-8, which officially operated on July 7, 2015, is the new generation geostationary meteorological satellite of Japan. It can provide observations every 10 min, and its observation range covers one-third of the earth. Besides, the spatial resolution of Himawari-8 is 0.5 km (red band), 1 km (blue, green, and NIR bands), and 2 km (other bands). Therefore, many researchers started to utilize Himawari-8 products to estimate and analyze PM_{2.5} recently. For example, Wang et al. derived hourly PM_{2.5} concentrations from Himawari-AODs over Beijing-Tianjin-Hebei in China (Wang et al., 2017). Zang et al. estimated hourly PM_{2.5} in China, and Xue et al. estimated hourly PM_{2.5} in central and eastern China (Xue et al., 2020; Zang et al., 2018).

Nevertheless, higher temporal resolution products that provide more details tend to distract researchers from larger-scale features. Meteorological conditions and PM_{2.5} concentrations change dramatically in a short period, but slowly and with apparent seasonal periodicity on a longer time scale (He et al., 2020). This long-term information, which may be beneficial for a more accurate estimation of PM_{2.5}, was usually overlooked. Long short-term memory network (LSTM) is good at processing short and long-term information and performs well in various sequential tasks (Fischer and Krauss, 2018; Tong and Sun, 2017). The specially

designed structure makes it store long-term information effectively and adjust the proportion of long-term information and short-term information timely according to the inputs of each time step (Pak et al., 2020). A few studies have applied LSTM to forecast PM_{2.5} concentration measurements of monitoring stations, helping people avoid possible serious air pollution. (Pak et al., 2020; Zhang et al., 2020). However, for researches focusing on epidemiology and meteorology, surface PM_{2.5} concentrations are superior to station data because of higher coverage. To the best of our knowledge, LSTM has not been utilized to estimate surface PM_{2.5} concentrations.

Therefore, this study aims to estimate surface PM_{2.5} concentrations using satellite observations, meteorological conditions via LSTM. Geospatial autocorrelation information was added to enhance the spatial ability of LSTM, forming the Geo-intelligent LSTM (Geoi-LSTM). We adopted station-based cross-validation (CV) and yearly-validation to evaluate our model and compared it with several popular models. Results based on the model were comprehensively analyzed to summarize the spatiotemporal pattern of PM_{2.5}. Hourly estimations and meteorological conditions were combined to explore the cause of short-term pollution event to show the potential on pollution mechanism research of our results.

2. Materials and methods

2.1. Study region and ground-level PM_{2.5} measurements

We chose Wuhan Urban Agglomeration (WUA) as our study region (Fig. 1), and the study period was the whole year of 2017. Besides, data in 2016 were also collected for yearly-validation. The WUA, which is the largest urban agglomeration in central China, refers to an urban cluster consisting of nine large and medium-sized cities (i.e., Wuhan, Huangshi, Ezhou, Huanggang, Xiaogan, Xianning, Xiantao, Qianjiang, Tianmen), with Wuhan as the central city and Huangshi as the sub-central city. WUA has been suffering severe air pollution in recent years. Therefore, it is urgent to study the PM_{2.5} pattern there.

Hourly PM_{2.5} concentration data within the study region in 2016 and 2017 were obtained from the China National Environmental Monitoring Center (CNEMC) website (<http://www.cnemc.cn>) and the Hubei Provincial Environmental Monitoring Center Station (HPEMCS) website (<http://www.hbemc.com.cn/>). In this study, all the stations in the latitude range of 28.5°–32°N and longitude range of 112.5°–116.25°E were used, including 76 CNEMC stations and 39 HPEMCS stations. The data from stations, whose records were less than 70% of a year, were removed to ensure the accuracy of measurements. The distribution of monitor stations is shown in Fig. 1.

2.2. Satellite observation

The Advanced Himawari Imager onboard Himawari-8 can provide the TOA reflectance at six visible or near-infrared wavelengths every 10 min. TOA reflectance is usually used to retrieve AOD by building a look-up table through an atmospheric radiative transfer model, and AOD is widely used to estimate PM_{2.5} (Belgiu and Drăguț, 2016; Liu et al., 2019b). However, affected by adverse factors (e.g., algorithm limitations and clouds coverage), AOD products have a large number of missing values (Song et al., 2019; Wang et al., 2019). Meanwhile, a few studies have proved that PM_{2.5} concentrations estimated directly from TOA reflectance have comparable accuracy and higher coverage than those from AOD (Shen et al., 2018). Therefore, Level 1B full-disk calibrated

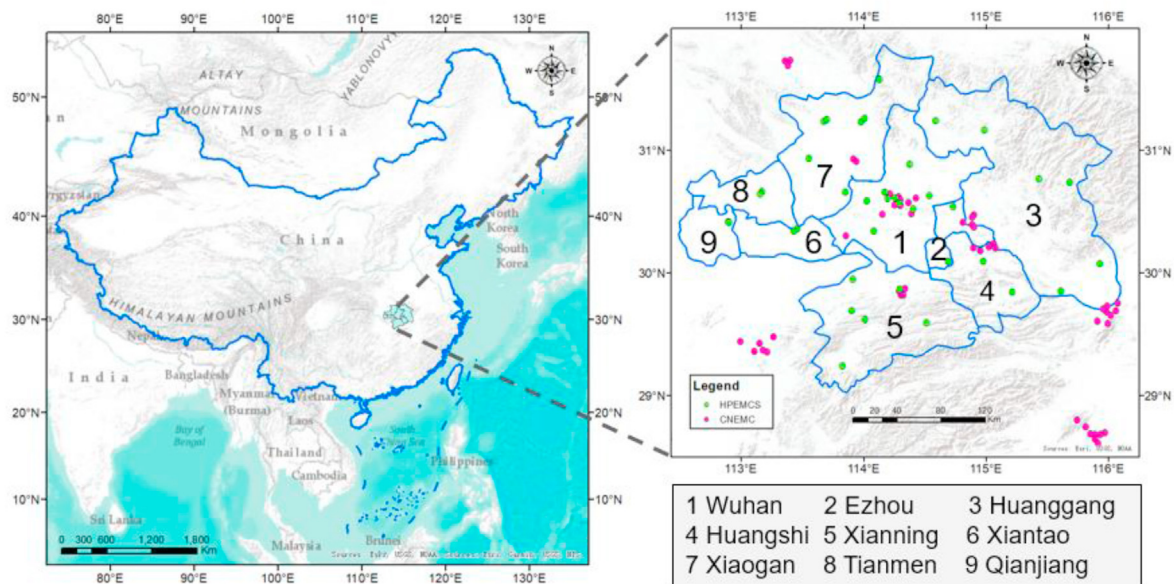


Fig. 1. Study region and distribution of PM_{2.5} monitoring stations. Green points represent HPEMCS stations; Pink points represent CNEMC stations. Blue curves represent the boundary of China (left) and WUA (right), respectively. Background maps depict the topography information of the study region. (For interpretation of the references to colour in this figure legend, the reader is referred to the Web version of this article.)

reflectance products with 5-km spatial resolution and 1-h temporal resolution were downloaded from the Japan Aerospace Exploration Agency P-Tree system (<ftp://ftp.ptree.jaxa.jp/>). The reflectance of band 1 (0.46 μm), band 3 (0.64 μm), band 6 (2.3 μm), and four observation angles (i.e., satellite zenith angle, SAZ; satellite azimuth angle, SAA; solar zenith angle, SOZ; and solar azimuth angle, SOA) were selected from the reflectance product because these are necessary parameters when retrieving AOD (Kaufman et al., 1997). These variables together are hereinafter referred to as TOA reflectance. In previous studies, AOD or cloud-removed TOA reflectance were usually chosen as the main predictor. However, we chose the original TOA reflectance instead of them because they have too many missing values (see more discussion in section 3.5 and Supplementary Data). Besides, level 2 AOD products, including AOD and Angstrom exponent (AE) information, were downloaded for comparison. Level 2 Cloud products were downloaded to distinguish cloud pixels and remove cloud-contaminated TOA reflectance.

2.3. Auxiliary data

Meteorological conditions and land cover data are widely used to estimate PM_{2.5} concentration as auxiliary variables (Stafoggia et al., 2019). Therefore, we downloaded The Modern Era Retrospective-analysis for Research and Applications version 2 meteorological reanalysis data, which includes temperature at 2 m above the ground (T2M, K), east and north wind speed at 10 m above the ground (U10M, V10M, m/s), pressure (PS, hpa), planetary boundary layer height (PBLH, m), and specific humidity (SH, g/kg) from the Goddard Earth Sciences Data and Information Services Center (<https://gmao.gsfc.nasa.gov/>). The spatial resolution is 0.5° by latitude and 0.625° by longitude, and the temporal resolution is hourly. Besides, we adopted NDVI products as an approximation of land use data. 16 days NDVI values (spatial resolution: 0.05°) in the study period were extracted from Moderate-resolution Imaging Spectroradiometer (MODIS) MYD13C1 datasets, which were downloaded from the Level 1 and Atmosphere Archive and Distribution System (<https://ladsweb.modaps.eosdis.nasa.gov/>).

2.4. Data integration

Firstly, the whole study region was divided into geographic grids with a spatial resolution of $0.05^\circ \times 0.05^\circ$ ($\approx 5 \text{ km} \times 5 \text{ km}$). Specifically, the study region was divided into 5250 ($75^\circ \times 70^\circ$) grids. Among them, 55 and 74 grids were assigned with PM_{2.5} monitoring stations in 2016 and 2017, respectively. We resampled all the auxiliary variables to a 5-km and hourly resolution via the bilinear interpolation method for the uniform resolution. After that, all the independent variables were matched to hourly PM_{2.5} concentrations of each monitoring station by grids. If there were more than one station in a grid, their measurements would be averaged to represent PM_{2.5} concentration in this grid. Then we calculated the geospatial autocorrelation grid by grid (see more in section 2.5). After exploring the optimal modeling strategy by testing different combinations of variables, we selected TOA reflectance, meteorological conditions, and NDVI as inputs (see more in Supplementary Data). Therefore, in our dataset, for a specific grid g and a specific timestep t , there is a unique record, including PM_{2.5} measurement, TOA reflectance, meteorological conditions, NDVI, and geospatial autocorrelation. All records in one grid were arranged in chronological order. This dataset would be used to estimate surface PM_{2.5} concentrations, and the data in grids, where there were monitoring stations, would be utilized to train and validate our models.

2.5. Geo-intelligent LSTM model for PM_{2.5} estimation

LSTM was developed by Hochreiter and Schmidhuber, and was designed to avoid the long-term dependency problem of standard recurrent neural network (RNN) caused by “vanishing gradient” (Hochreiter and Schmidhuber, 1997). LSTM consists of the same units, which also be called cells. The structure of a cell in LSTM is shown in Fig. 2a. As shown, all information flow along the horizontal line running through the top of the diagram, which is called “cell state” (C_t in Fig. 2a). Many cells are connected through the cell state to form an LSTM layer (Fig. 2b). The ability to remove or add information to the cell state is carefully regulated by structures called gates, composed of a sigmoid neural net layer and a

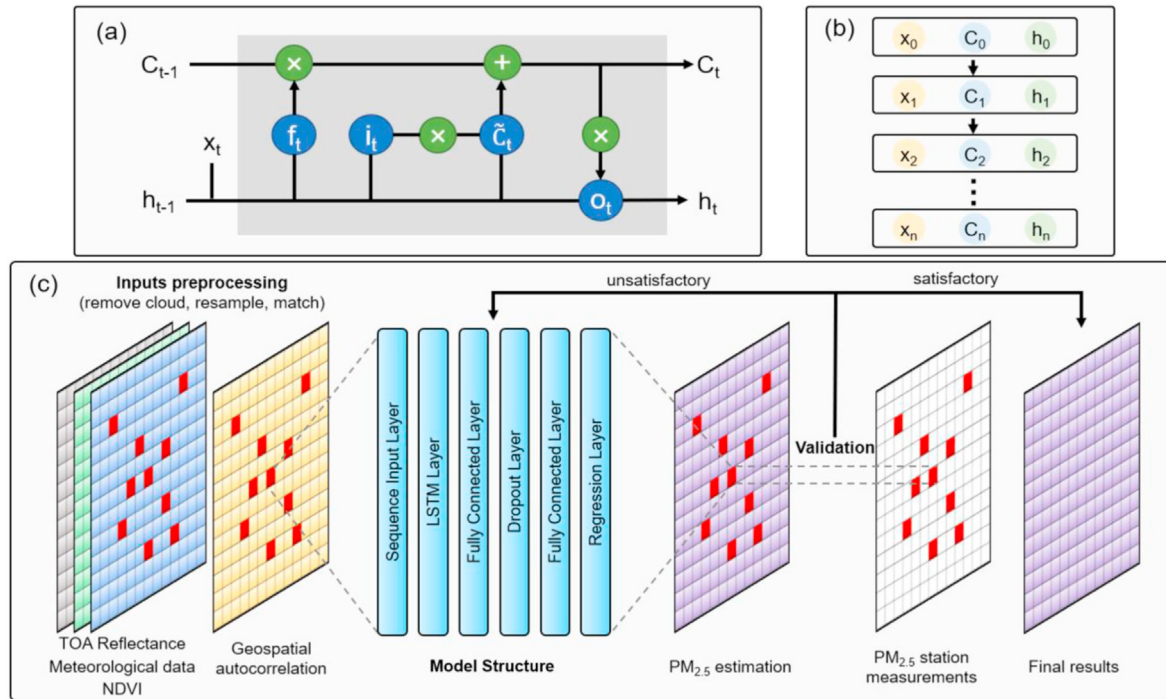


Fig. 2. The framework of Geoi-LSTM. (a) The structure of an LSTM cell. (b) The formation of an LSTM layer. (c) The framework of the Geoi-LSTM applied to estimate $PM_{2.5}$ concentrations.

pointwise multiplication operation.

There are three gates in each cell of LSTM. Firstly, the “forget gate layer” (f_t in Fig. 2a) decides what information should be thrown away from the cell state according to equation (1). The next step is to decide what new information should be stored in the cell state, which is executed by the “input gate layer” (i_t in Fig. 2a) according to equation (2) ~ (3). Then the forgetting and inputting process will be executed according to equation (4). Finally, the “output gate layer” (o_t in Fig. 2a) decides what should be output according to equation (5) ~ (6).

$$f_t = \sigma(W_f \cdot [h_{t-1}, x_t] + b_f), \quad (1)$$

$$i_t = \sigma(W_i \cdot [h_{t-1}, x_t] + b_i), \quad (2)$$

$$\tilde{C}_t = \tanh(W_C \cdot [h_{t-1}, x_t] + b_C), \quad (3)$$

$$C_t = f_t * C_{t-1} + i_t * \tilde{C}_t, \quad (4)$$

$$o_t = \sigma(W_o \cdot [h_{t-1}, x_t] + b_o), \quad (5)$$

$$h_t = o_t * \tanh(C_t), \quad (6)$$

where f_t , i_t , o_t , h_t , x_t represent forget gate layer, input gate layer, output gate layer, output value, and input variables of the t th cell, respectively; C_t and \tilde{C}_t represent cell state and candidate values that could be added to cell state of t th cell, respectively. W and b represent the corresponding calculations' weights and offsets; $\sigma(\cdot)$ represents sigmoid function, and $\tanh(\cdot)$ represents hyperbolic tangent function; t represents the timestep.

The distribution pattern of $PM_{2.5}$ has significant spatiotemporal autocorrelation, which means that for a specific grid and a specific hour, the $PM_{2.5}$ measurements in nearby grids and the $PM_{2.5}$

measurements in the past hours or days in the same grid are informative for estimation (Li et al., 2017b). LSTM can make full use of temporal features of datasets throughout its special structure, but cannot extract the spatial characteristics. Therefore, we added geospatial autocorrelation into LSTM to develop a Geo-intelligent LSTM (Geoi-LSTM), making up that shortcoming. For a specific hour in each grid, this term was calculated by:

$$G_{PM_{2.5}} = \frac{\sum_{i=1}^m w_{s,i} PM_{2.5,i}}{\sum_{i=1}^m w_{s,i}} \quad \text{and} \quad w_{s,i} = \frac{1}{d_{s,i}^2}, \quad (7)$$

where $G_{PM_{2.5}}$ represents geospatial autocorrelation; i represents grid where there exists monitoring station and the $PM_{2.5,i}$ represents the measurement of the station. $d_{s,i}$ represents the spatial distance between grid i and target grid; m represents the number of nearby stations used to calculate geospatial autocorrelation. In this study, the parameter m was set as 12 after experiments (Table S2).

The structure of Geoi-LSTM is shown in Fig. 2c. The inputs include TOA reflectance, meteorological data, NDVI, and geospatial autocorrelation. The model consists of a sequence input layer, whose size equals the feature dimensions of inputs; an LSTM layer, which has 300 cells; a fully connected layer, whose size is 100; a dropout layer with a dropout rate of 0.3; a fully connected layer, whose size equals to the feature dimensions of output; and a regression layer, whose loss function is mean squared error.

2.6. Model validation

As described above, LSTM can learn long-term information from the dataset, which is beneficial to improving performance. Therefore, we inputted a dataset, which is the same as described in the Data integration section but disordered, to the LSMT and Geoi-LSTM model to explore how long-term information is essential and examined the effectiveness of geospatial autocorrelation.

Besides, the overfitting issue has been an inescapable problem since machine learning methods have occurred. The dropout method developed by Srivastava et al. (2014) was turned out to be an effective way to avoid overfitting (Yan et al., 2020a). Therefore, we added a dropout layer in our model and conducted a contrast experiment that trained the model without a dropout layer to examine its effectiveness on the PM_{2.5} estimation task.

Sample-based CV is a widely used validation approach, but it will shuffle the data, thus breaking the time continuity and long-term information. Therefore, we used the station-based CV instead, which can more accurately reflect the spatial performance of the model (Wei et al., 2019). For the station-based CV, we randomly isolated one-fold stations first and trained the model with the data of left nine-fold stations, and then evaluated model performance using the isolated data. This process was repeated 10 times to ensure that all the stations had been examined. However, this process cannot ensure that the data samples for model training and validation are entirely independent on both spatial and temporal scales, which can be remedied by yearly-validation (Liu et al., 2020; Yan et al., 2020b). Specifically, we downloaded data in 2016, implemented the same preprocessing as data in 2017. Then we trained the model using data in 2017 and validate the model using data in 2016. Several widely used statistical indicators were selected to quantify the performance of the models: the coefficient of determination (R^2), root mean squared error (RMSE) and mean absolute error (MAE). They are defined as the following equations:

$$R^2 = 1 - \frac{\sum_{i=1}^n (PM_{2.5}^{mea}(i) - PM_{2.5}^{est}(i))^2}{\sum_{i=1}^n (PM_{2.5}^{mea}(i) - \overline{PM_{2.5}^{mea}})^2}, \quad (9)$$

$$RMSE = \sqrt{\frac{1}{n} \sum_{i=1}^n (PM_{2.5}^{mea}(i) - PM_{2.5}^{est}(i))^2}, \quad (10)$$

$$MAE = \frac{1}{n} \sum_{i=1}^n |PM_{2.5}^{mea}(i) - PM_{2.5}^{est}(i)|, \quad (11)$$

where n is the total number of samples, $PM_{2.5}^{mea}$ and $PM_{2.5}^{est}$ represent ground-level PM_{2.5} concentration measurements and model estimated PM_{2.5} concentrations, respectively. $\overline{PM_{2.5}^{mea}}$ is the mean value of the ground-level PM_{2.5} concentration measurements.

3. Results and discussion

3.1. Validation results of Geoi-LSTM

We conducted contrast experiments to verify the effectiveness of Geoi-LSTM, and the results are shown in Table 1. The Geoi-LSTM with ordered inputs achieved the best performance, with station-based CV R^2 , RMSE, MAE of 0.82, 15.44 $\mu\text{g}/\text{m}^3$, 10.63 $\mu\text{g}/\text{m}^3$, respectively, and yearly-validation R^2 , RMSE, MAE of 0.59, 22.05 $\mu\text{g}/\text{m}^3$.

Table 1
Validation results of models.

Models	Station-based CV (N = 208,826)			Yearly-validation (N = 151,987)		
	R^2	RMSE	MAE	R^2	RMSE	MAE
LSTM (disordered)	0.52	25.24	17.36	0.15	44.19	33.28
LSTM	0.71	19.04	13.02	0.45	25.48	18.51
Geoi-LSTM (disordered)	0.69	20.72	13.64	0.41	28.58	20.42
Geoi-LSTM	0.82	15.44	10.63	0.59	22.05	15.44

The unit of RMSE and MAE is $\mu\text{g}/\text{m}^3$.

m^3 , 15.44 $\mu\text{g}/\text{m}^3$, respectively. For all models, station-based CV performances were better than yearly-validation, which is because the training data and validation data are entirely independent in yearly-validation so that the model can not learn the full features. This phenomenon was also reported by other researchers (Wei et al., 2019; Liu et al., 2020). As described in the Materials and methods section, LSTM can learn long-term information from the dataset. Therefore, disordered inputs, which means the long-term features were broken, caused the statistical indicators of both LSTM and Geoi-LSTM decreasing as expected. Besides, Geoi-LSTM performed better than LSTM in all cases, especially when the inputs were disordered. The results suggested that the geospatial autocorrelation played an essential role in PM_{2.5} estimation, especially when temporal information was broken.

Besides, we conducted contrast experiments with many different parameter settings to verify the effectiveness and necessity of the dropout layer in Geoi-LSTM. The results are shown in Table S2. It can be found that the difference between training results and station-based CV results was smaller when the dropout layer exists, which suggested it overcome the overfitting issue effectively. For example, when the value of m was 12, and the number of cells was 300, the training R^2 was both 0.83 with or without the dropout layer. The station CV R^2 was 0.71 without the dropout layer, while the station CV R^2 was 0.82 with the dropout layer.

As shown in Table 1, the Geoi-LSTM achieved the most satisfactory performance. Therefore, we drew scatter plots of the results at different temporal scales (i.e., hourly, daily, monthly) to comprehensively display its validation results (Fig. 3). Overall, our model performed satisfied at different time scales. Specifically, the hourly, daily, and monthly station-based CV R^2 was 0.82, 0.87, and 0.93, respectively. And the corresponding value of yearly-validation was 0.59, 0.64, and 0.67, respectively. Models performed better at a coarser time scale because the average can eliminate random error partly, improving the accuracy of estimations. Furthermore, we displayed station-based CV results of different hours and different seasons separately (Figs. S1–2). As shown, the statistical indicators and sample distributions of hourly results were very close. R^2 of different hours were between 0.78 and 0.83, RMSE of them were between 14.7 $\mu\text{g}/\text{m}^3$ and 18.17 $\mu\text{g}/\text{m}^3$, and MAE of them were between 10.26 $\mu\text{g}/\text{m}^3$ and 12.31 $\mu\text{g}/\text{m}^3$. However, validation results were highly distinct in different seasons (Fig. S2). Accuracy in summer was worse than in other seasons, with an R^2 of 0.64. Besides, the concentrations were closer and smaller in summer, while more disperse and larger in winter. In all scatter plots, the slopes of the regression line were less than 1, suggesting that the models underestimated high values, which was also reported by other researchers (Fang et al., 2016; You et al., 2016). For more discussion about the possible reasons and the effect of meteorological conditions, please refer to Fig. S3 and Supplementary Data.

Moreover, we displayed temporal plots for typical stations at a daily scale to further examine Geoi-LSTM's temporal performance (Qin et al., 2019; Wu and Lin, 2019). As shown in Fig. S4, the ranges of R^2 , RMSE, and MAE were 0.64–0.93, 9.38–16.99 $\mu\text{g}/\text{m}^3$, 6.77–12.21 $\mu\text{g}/\text{m}^3$. Large errors were usually found when the measurement values were high or there were many missing data. It is difficult for the model to learn the characteristics of too high values because of the lack of samples (see more in Supplementary Data). In summary, the estimations and measurements showed excellent consistency. We also calculated the differences between annual averaged estimations and station measurements to examine Geoi-LSTM's spatial performances. As shown in Fig. S5, relatively large errors occur in a few stations, while most of the estimations are consistent with measurements. Specifically, 51.1% of the annual differences are between -3 and 3 $\mu\text{g}/\text{m}^3$, 7.8% of values are less

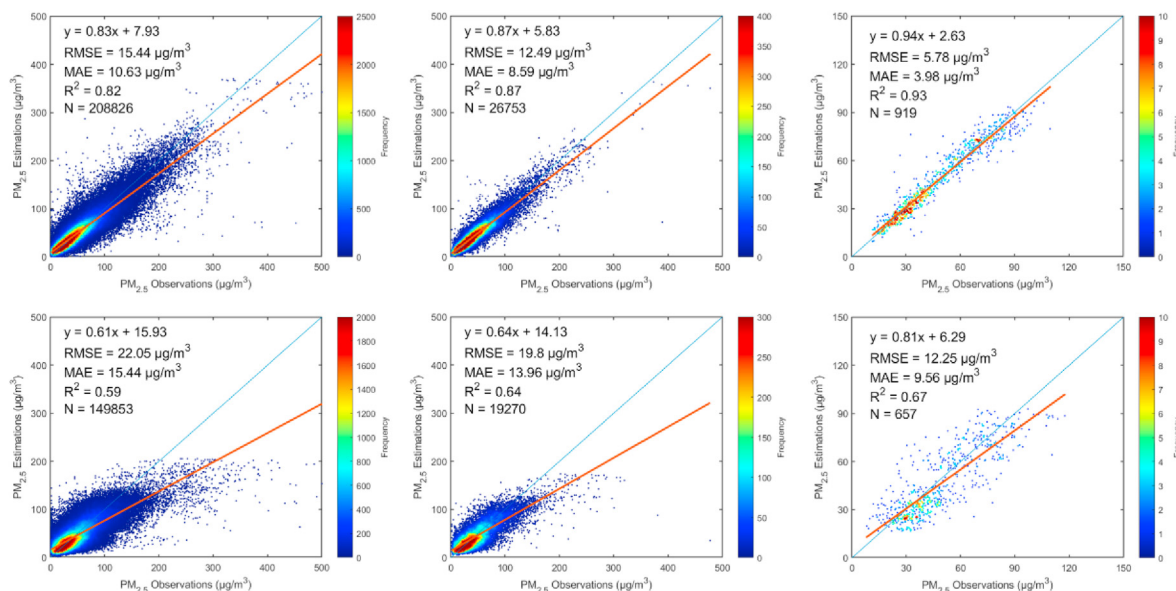


Fig. 3. The station-based CV and yearly-validation results of Geoi-LSTM. (a–c) Hourly, daily, and monthly scatter plots of station-based CV. (d–f) Hourly, daily, and monthly scatter plots of yearly-based validation. The horizontal axis shows the ground-level station $PM_{2.5}$ observations, and the vertical axis shows the $PM_{2.5}$ concentrations estimated by the model. Blue lines in scatter plots represent the 1:1 reference line, and red lines represent the regression line of measurements and estimations. (For interpretation of the references to colour in this figure legend, the reader is referred to the Web version of this article.)

than $-9 \mu\text{g}/\text{m}^3$, and only 2.2% of values are more than $9 \mu\text{g}/\text{m}^3$. As for the spatial pattern, estimations are more accurate in the eastern and western WUA. The larger errors are mainly located at Xiaogan city, which implies that the model cannot learn enough characteristics of $PM_{2.5}$ in Xiaogan from the data because of the sparse distribution of stations. As stated above, the $PM_{2.5}$ concentrations estimated by Geoi-LSTM and $PM_{2.5}$ concentrations measured by monitoring stations were highly consistent both in space and time.

3.2. Spatiotemporal characteristics of estimated $PM_{2.5}$

The hourly and annual averaged $PM_{2.5}$ concentrations are shown in Fig. 4. A slight uptrend in the morning and a downtrend in the afternoon can be discovered even though the differences are not that great, which can also be found in station measurements (Fig. S6). Specifically, the mean $PM_{2.5}$ concentrations from 0900 local time (LT) to 1600 LT are 49.57, 49.92, 50.21, 49.3, 47.53, 45.5, 43.43, $42.35 \mu\text{g}/\text{m}^3$, respectively. In the morning, $PM_{2.5}$ concentrations are relatively high in most areas of WUA, except two small mountainous areas in the southern and northeastern (Fig. 1). $PM_{2.5}$ concentrations reach a peak at 1200 LT, and the most polluted area is the junction of Jingzhou city, Huanggang city, and Huangshi city, followed by Wuhan city and Xiaogan city. (Fig. 4d). In the afternoon, the concentrations decline significantly in the central and north-western areas, especially in Wuhan city, whereas the junction area still maintains a relatively high concentration level.

The spatial characteristics of seasonally averaged $PM_{2.5}$ concentrations are more ambiguous than those of hours, while the temporal characteristics are much more distinct (Fig. 5). Specifically, Summer is the cleanest season, with an averaged $PM_{2.5}$ concentration of $27.46 \mu\text{g}/\text{m}^3$, and winter is the most polluted season, with an averaged $PM_{2.5}$ concentration of $74.28 \mu\text{g}/\text{m}^3$. Spring and autumn have comparable levels of pollution. The averaged $PM_{2.5}$ concentrations are $46.10 \mu\text{g}/\text{m}^3$ and $41.23 \mu\text{g}/\text{m}^3$, respectively. These conclusions are consistent with station measurements (Fig. S6).

To find out the factors behind these spatiotemporal patterns, we

calculated hourly and seasonally averaged meteorological conditions, shown in Fig. S6. Hourly temperature and PBLH have a similar variation trend that increases before 1400 LT and decreases after that. Even though the range of variation in temperature is narrow, the rises of temperature and PBLH usually enhance air convective motion and diffuse the pollution (Luo et al., 2017). Averaged wind speeds in WUA at different hours are all below 1 m/s, lower than most regions in China (Liu et al., 2019a). Pressure decreases monotonically, but specific humidity increases monotonically. The former benefits $PM_{2.5}$ diffusion, while the latter benefits $PM_{2.5}$ deposition (Li et al., 2015; Luo et al., 2017). As shown in Fig. S6, meteorological conditions change more dramatically with the seasons. Both temperature and specific humidity are higher in summer and lower in winter, while the pressure is contrary. PBLH decreases monotonically, but the magnitude is not large enough compared to hourly results. Wind speeds are very low in spring, with a value of 0.48 m/s, and still less than 2 m/s in autumn. The variation trends of seasonal $PM_{2.5}$ concentrations are consistent with temperature, specific humidity, and pressure. Except for meteorological conditions, emission also contributed to the $PM_{2.5}$ pattern. For example, traffic-related $PM_{2.5}$ is higher in the morning rush hour because of commuting (Jeong et al., 2019). Moreover, vehicle emission, biomass burning, fireworks will produce more $PM_{2.5}$ concentrations in winter than other seasons in WUA (Wang et al., 2020).

3.3. Application of hourly $PM_{2.5}$ in pollution event analysis

Compared to daily $PM_{2.5}$ concentrations, hourly results reveal more details on temporal variation. Scores of pollution events that are short-lived but reached very high concentration levels can be detected by our results, which may seem ambiguous in daily results. To demonstrate the potential of hourly results, we conducted a pollution event analysis using the distribution of surface $PM_{2.5}$ concentration estimated by the constructed Geoi-LSTM model for the designated local time on May 6, 2017, combined with meteorological conditions. We analyzed several common meteorological

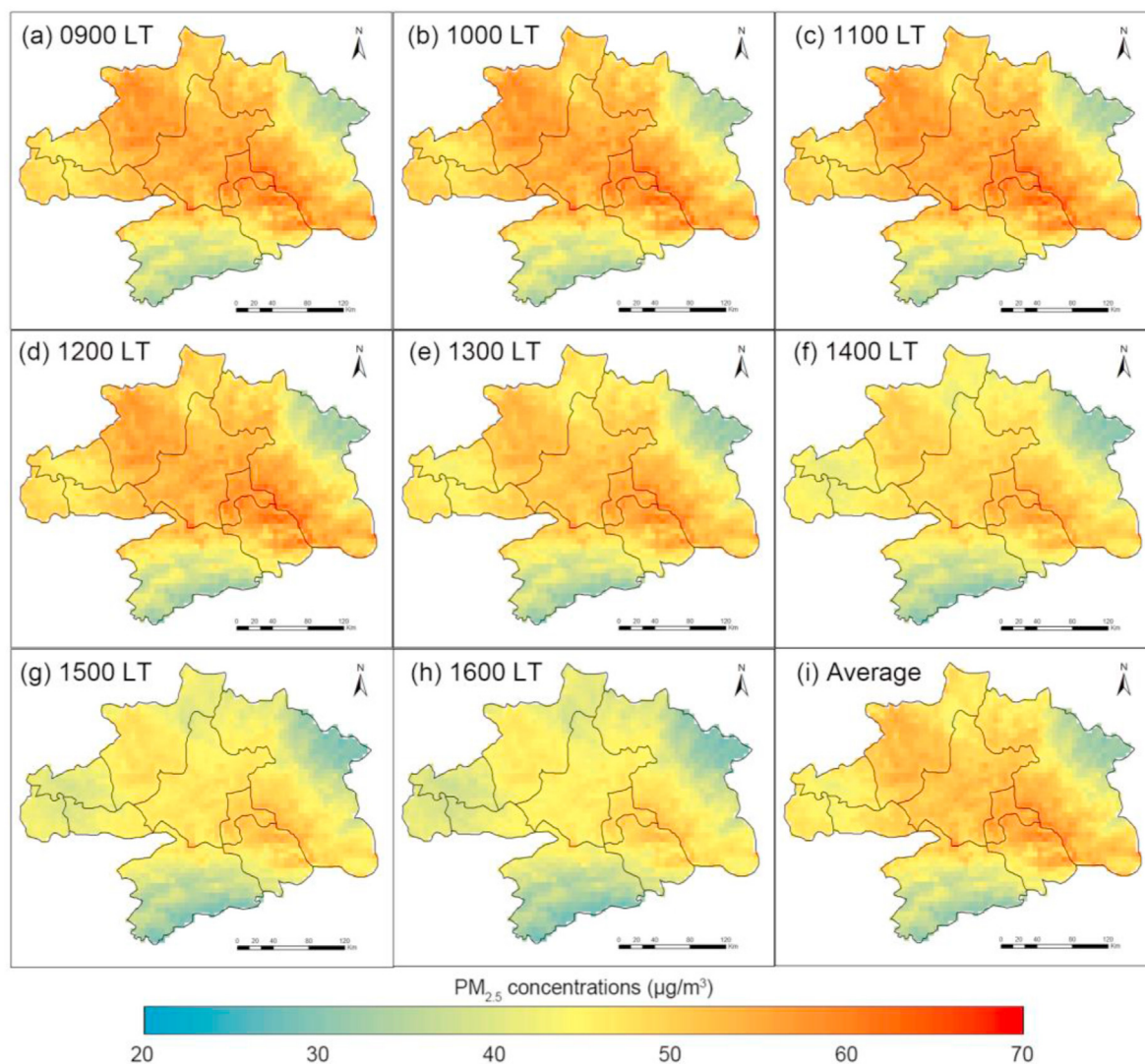


Fig. 4. Spatial distribution averaged $PM_{2.5}$ concentrations in each hour in WUA derived from Geoi-LSTM. (a–h) Hourly averaged $PM_{2.5}$ concentrations. (i) Annual averaged $PM_{2.5}$ concentrations.

variables, including PBLH, wind, surface pressure, which are highly correlated with $PM_{2.5}$ concentrations (Stafoggia et al., 2019).

Fig. 6 displays the process of a pollution event and corresponding meteorological conditions. Considering the time-lag effect, meteorological conditions for each hour are connected to the $PM_{2.5}$ concentration of the next hour. As shown, this event erupts in central WUA because of unfavorable anthropogenic and meteorological conditions. On the one hand, Wuhan city has more emissions than other surrounding cities due to its relatively high urbanization level. On the other hand, there are mountains and hills to the northwestern, northeastern, and southern WUA (Fig. 1), creating a high-pressure belt (Fig. 6a), which is often accompanied by high $PM_{2.5}$ concentration (Yang et al., 2017), in the central and western WUA. At 0900 LT, the PBLH in central and western WUA is less than 300 m, and in some places as low as 20 m (Fig. 6a). Therefore, plenty of $PM_{2.5}$ produced by industries and residential activities have no opportunity for vertical diffusion. The wind in central and western WUA are mainly from the north and northeast, and the wind speeds are quite low (less than 3 m/s). All these conditions shape the outbreak area into a belt. By 1200 LT, PBLH raises to about 1000 m, while the wind field has no obvious

variation (Fig. 6c). Consequently, the $PM_{2.5}$ concentrations decrease overall, but the shape of the outbreak area remains unchanged. That is, $PM_{2.5}$ spreads vertically but remains stable horizontally. However, it should be noted that a small amount of pollution in western WUA spread to southwestern WUA under the influence of persistent south winds (Fig. 6d). In the afternoon, PBLH continues to rise slightly, the wind directions change to north and northwest, and the wind speeds increase significantly. Accordingly, $PM_{2.5}$ significantly decreases in central and western WUA and slightly increases in southern and southeastern WUA. The distribution of $PM_{2.5}$ is more even, and the concentration values are smaller on the whole, which means the pollution dissipated eventually. Station measured $PM_{2.5}$ concentrations, the model estimated $PM_{2.5}$ concentrations, and meteorological conditions are highly consistent during this process, which exhibits the potential of our results on short-term pollution event research.

3.4. Loss in the process of cloud removal

Clouds can reflect electromagnetic waves and thus weaken the correlation between $PM_{2.5}$ and satellite observations. When

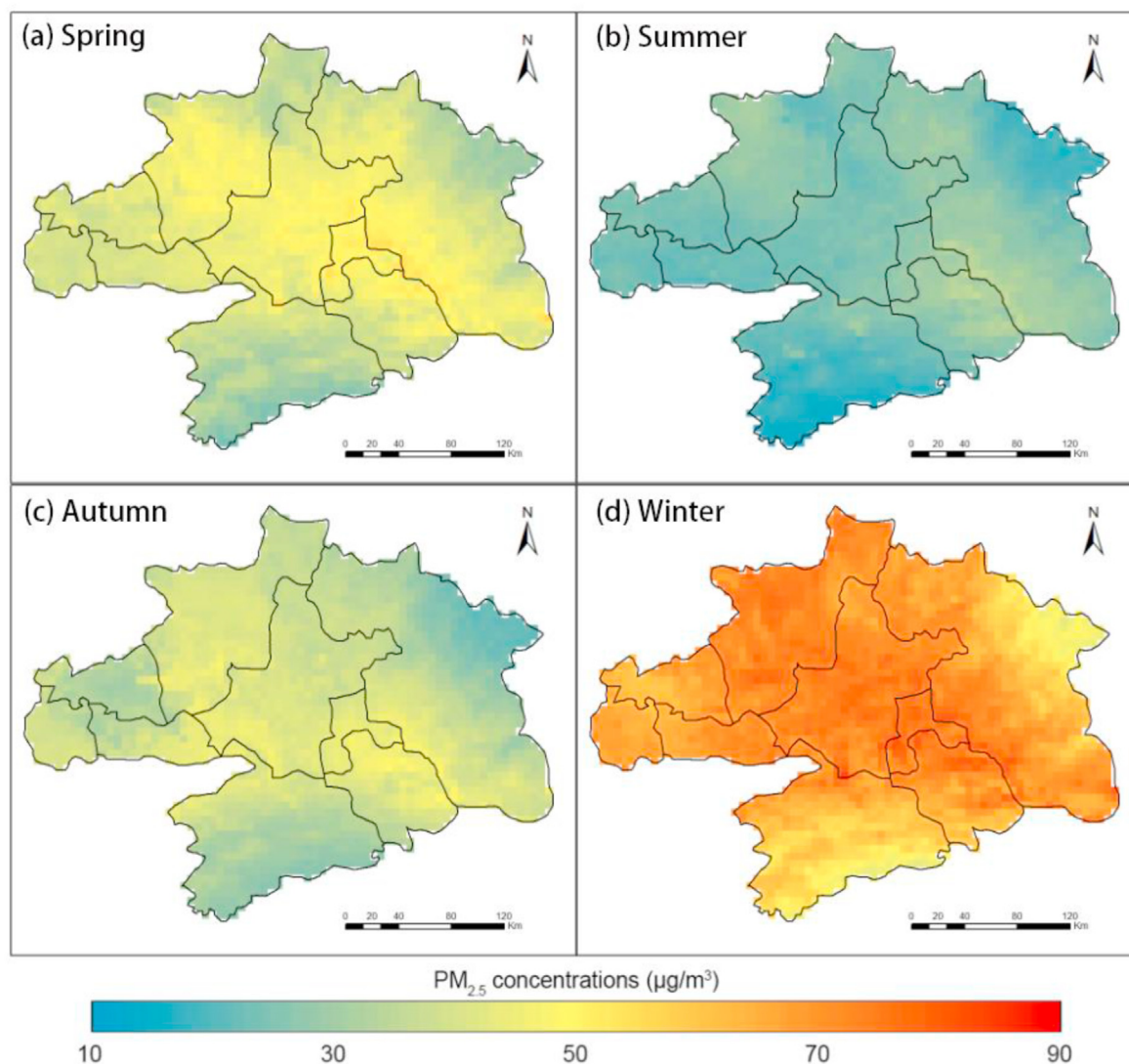


Fig. 5. Spatial distribution of averaged $PM_{2.5}$ concentration in each season in WUA derived from Geoi-LSTM. (a) Spring (i.e., March, April, May). (b) Summer (i.e., June, July, August). (c) Autumn (i.e., September, October, November). (d) Winter (i.e., December, January, February).

retrieving AOD, the pixels covered by clouds will be regarded as invalid. Several previous studies used TOA reflectance instead of AOD to exclude cloud-covered pixels as well (Liu et al., 2019b; Shen et al., 2018). However, we chose to use original TOA reflectance because there are too many missing values in AOD and cloud-removed TOA reflectance (Song et al., 2019). As shown in Table S1, the model using original TOA reflectance as inputs achieved better performance than using cloud-removed TOA reflectance. This may be because high levels of $PM_{2.5}$ can sometimes be mistaken for clouds, and there are complex interactions among $PM_{2.5}$, aerosols, and clouds. Therefore, deleting pixels covered by clouds could reduce not only wrong information but also useful information. AOD was widely used to estimate $PM_{2.5}$ concentrations but performs poorly in our study because there are too many missing values in the Himawari-8 AOD product (Table S1). Specifically, the number of AOD records is 6% of TOA and 25% of cloud-removed TOA in WUA in 2017. Missing data reduces effective information and breaks the continuity of temporal variation, which impair model performance. The cloud coverages in the training dataset in spring, summer, autumn, and winter were 73.4%, 78.5%, 72.5%, 60.4%, respectively. Therefore, except for model

performance, cloud removal also damages the availability of results. Taking the pollution event shown in Fig. 6 as an example, we applied a cloud mask and a valid-AOD mask to the original $PM_{2.5}$ estimation results to show the differences. As shown in Fig. 7, the $PM_{2.5}$ concentrations become fragmentary after removing cloud-covered pixels, and only several pixels remain if we exclude AOD-invalid pixels. No evidence of the short-term pollution event can be found from these results, let alone variation patterns. In contrast, a complete and clear picture of the whole process of the event can be displayed based on our results (Fig. 6).

However, the comparison is only conducted in WUA, and it is to be verified whether more error information or more valid information is deleted during the cloud removal process in other regions, especially where often covered by thick clouds. Cloud removal is still a crucial process for ensuring the accuracy of estimation before sufficient verifications.

3.5. Comparison with other popular models

To make a comprehensive and fair comparison, we selected several popular algorithms to train the same datasets and validate

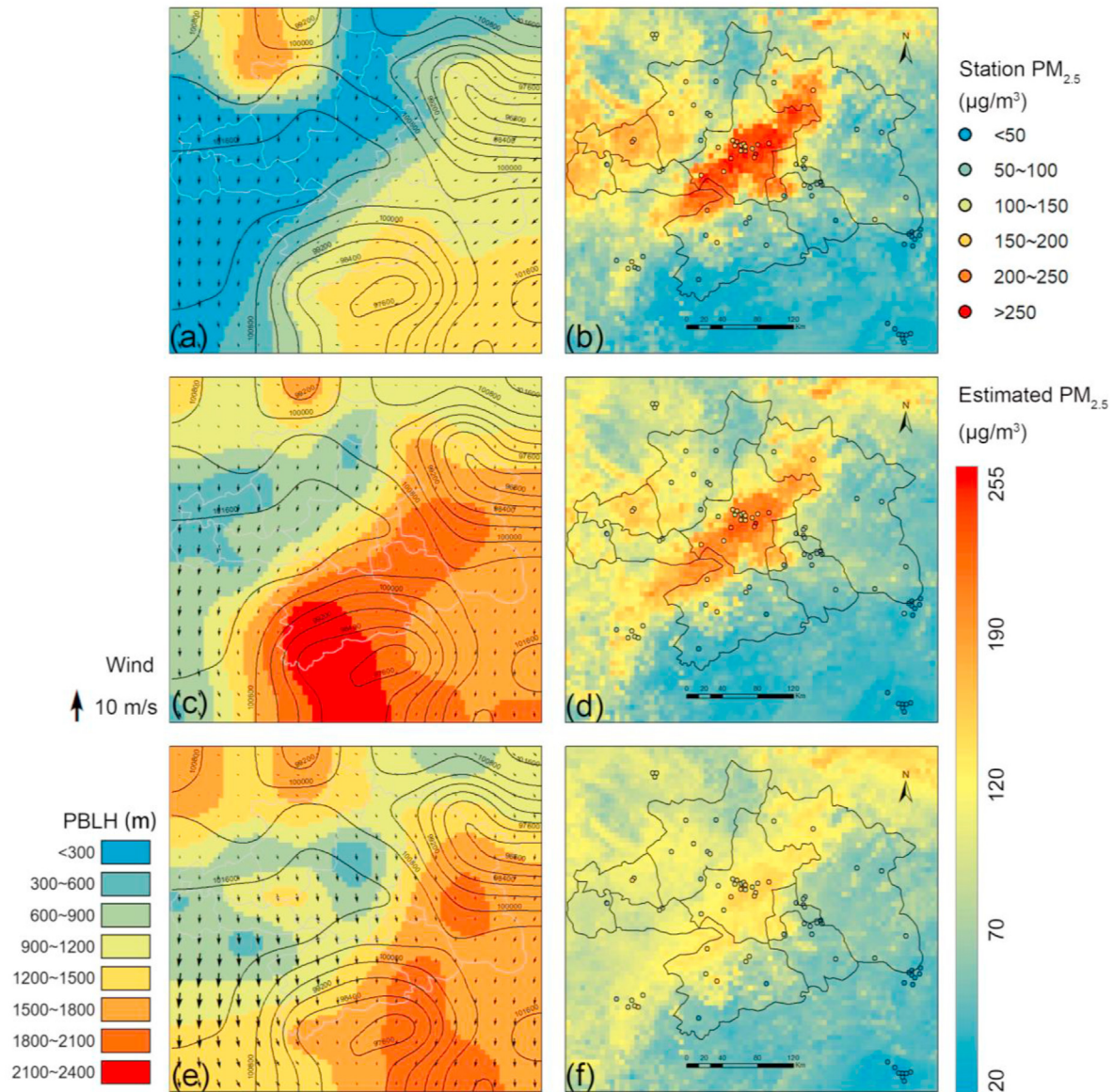


Fig. 6. Pollution event on May 6, 2017. Panels (a), (c), and (e) describe meteorological conditions at (a) 0900 LT, (c) 1200 LT, (e) 1500 LT. The background represents PBLH; arrows indicate wind fields; black curves represent the surface pressure isoline. Panels (b), (d), and (f) describe PM_{2.5} concentrations at (b) 1000 LT, (d) 1300 LT, (f) 1600 LT. The background represents the distribution of surface PM_{2.5} concentration estimated by the constructed Geoi-LSTM model for the designated local time on May 6, 2017, and points indicate PM_{2.5} concentrations measured by monitoring stations.

the performance using station-based CV uniformly. These algorithms, including GWR, LME, RF, and GRNN, were widely used in PM_{2.5} estimation and turn out to be effective (Shin et al., 2020). We also established an MLR model as the baseline reference. Those methods are detailed in the Supporting Information. As shown in Table 2, MLR exhibits the worst performance because of the simple structure and lacking learning ability. Results of GWR are a little better than MLR, with station-based CV R² of 0.33, RMSE of 30.45 μg/m³, and MAE of 20.81 μg/m³. The station-based CV R², RMSE, and MAE of LME are 0.73, 18.15 μg/m³, and 12.27 μg/m³. The yearly-validation R², RMSE, and MAE of LME are 0.46, 25.44 μg/m³, and 20.36 μg/m³. RF and GRNN have closely station-based CV results, but the latter performs better in yearly-validation. The comparison results indicate that our model's station-based CV MAE is slightly higher than that of RF. Except that, our model (i.e., Geoi-LSTM) achieved the best performance among all models.

4. Conclusion

In this study, we developed a geo-intelligent LSTM model to estimate hourly PM_{2.5} concentrations in WUA. We evaluated our model using two validation methods at hourly, daily, and monthly scale to examine it both in space and time. The results showed that estimations and measurements were highly consistent, with station-based CV R², RMSE, MAE of 0.82, 15.44 μg/m³, 10.63 μg/m³, respectively, and yearly-validation R², RMSE, MAE of 0.59, 22.05 μg/m³, 15.44 μg/m³, respectively. Though the benefits and loss from cloud removal in other regions need further verifications, our model performs satisfactorily with original TOA reflectance as inputs. Based on our results, we analyzed the spatiotemporal characteristics of PM_{2.5} concentrations in WUA and further researched the mechanism of a short-term pollution event. In short, hourly PM_{2.5} concentrations vary slowly, with a relatively high level in the

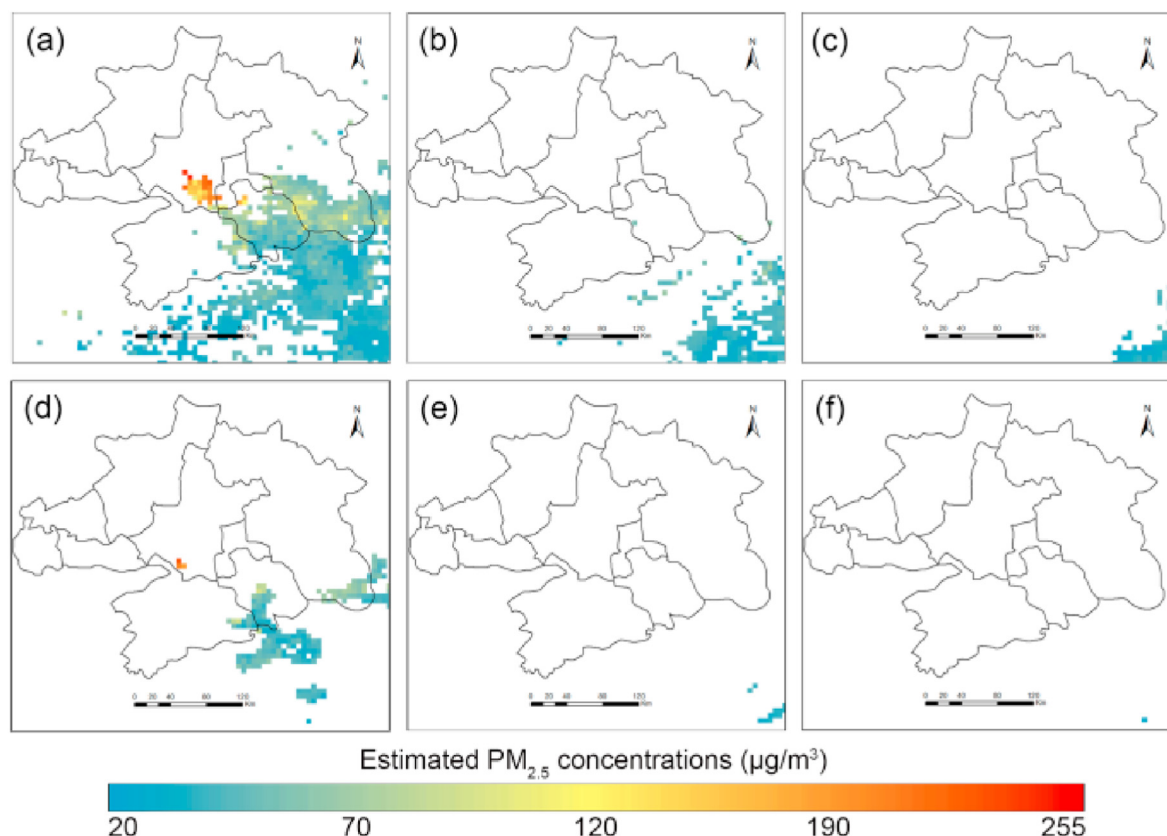


Fig. 7. The coverage of hourly results on May 6, 2017. (a), (b), (c) are the results that exclude pixels covered by cloud at 1000 LT, 1300 LT, 1600 LT, respectively. (d), (e), (f) are the results that exclude pixels where AOD are invalid, at 1000 LT, 1300 LT, 1600 LT, respectively.

Table 2
Validation results of different models.

Models	Station-based CV			Yearly-validation		
	R ²	RMSE	MAE	R ²	RMSE	MAE
MLR	0.29	33.06	23.45	0.20	30.75	24.56
GWR	0.33	30.45	20.81	0.26	29.53	23.38
LME	0.73	18.15	12.27	0.46	25.44	20.36
RF	0.80	15.65	10.21	0.51	24.06	17.95
GRNN	0.79	17.32	11.58	0.57	22.53	17.22
Geoi-LSTM	0.82	15.44	10.36	0.59	22.05	15.44

The unit of RMSE and MAE is $\mu\text{g}/\text{m}^3$.

morning and a low level in the afternoon. Seasonal $\text{PM}_{2.5}$ concentrations change more dramatically. Summer is cleanest; winter is most polluted; spring and autumn are in-between. The most pollutant area in WUA is the junction of Jingzhou city, Huanggang city, and Huangshi city. Compared to previous studies, our results can reflect details about variation patterns accurately and seamlessly, which can be more efficiently utilized by researchers of atmospheric science and human health.

Author contributions

Wang Bin: Data curation, Methodology, Formal analysis, Writing - original draft, Writing - Review & Editing. **Yuan Qiang-qiang:** Conceptualization, Funding acquisition, Project administration, Writing - Review & Editing. **Yang Qianqian:** Visualization, Investigation. **Zhu Liye:** Resources. **Li Tongwen:** Validation. **Zhang Liangpei:** Supervision.

Funding sources

We gratefully acknowledge the support from the Strategic Priority Research Program of the Chinese Academy of Sciences (No.XDA19090104), the National Natural Science Foundation of China (Nos. 41922008 and 41975139), the Fundamental Research Funds for the Central Universities of Wuhan University (No.2042019kf0213), and the Nature Science Foundation of Guangdong Province (No.2020A1515011133).

Declaration of competing interest

The authors declare that they have no known competing financial interests or personal relationships that could have appeared to influence the work reported in this paper.

Appendix A. Supplementary data

Supplementary data to this article can be found online at <https://doi.org/10.1016/j.envpol.2020.116327>.

References

- Belgiu, M., Drăguț, L., 2016. Random forest in remote sensing: a review of applications and future directions. *ISPRS J. Photogrammetry Remote Sens.* 114, 24–31. <https://doi.org/10.1016/j.isprsjprs.2016.01.011>.
- Chen, S., Oliva, P., Zhang, P., 2018. Air pollution and mental health: evidence from China. In: Presented at the National Bureau of Economic Research, 1050 Massachusetts Avenue Cambridge, MA, 2018, 24686. <https://www.nber.org/papers/w24686>. (Accessed 24 August 2019).
- Eslami, E., Salman, A.K., Choi, Y., Sayeed, A., Lops, Y., 2019. A data ensemble approach for real-time air quality forecasting using extremely randomized trees and deep neural networks. *Neural Comput. Appl.* 32, 7563–7579. <https://doi.org/10.1007/s00521-019-04500-0>.

- doi.org/10.1007/s00521-019-04287-6.
- Fang, X., Zou, B., Liu, X., Sternberg, T., Zhai, L., 2016. Satellite-based ground PM_{2.5} estimation using timely structure adaptive modeling. *Remote Sens. Environ.* 186, 152–163. <https://doi.org/10.1016/j.rse.2016.08.027>.
- Fischer, T., Krauss, C., 2018. Deep learning with long short-term memory networks for financial market predictions. *Eur. J. Oper. Res.* 270 (2), 654–669. <https://doi.org/10.1016/j.ejor.2017.11.054>.
- Gupta, P., Christopher, S.A., 2009. Particulate matter air quality assessment using integrated surface, satellite, and meteorological products: multiple regression approach. *J. Geophys. Res.* 114 (D14) <https://doi.org/10.1029/2008jd011496>.
- He, Q., Gu, Y., Zhang, M., 2020. Spatiotemporal trends of PM_{2.5} concentrations in central China from 2003 to 2018 based on MAIAC-derived high-resolution data. *Environ. Int.* 137, 105536 <https://doi.org/10.1016/j.envint.2020.105536>.
- Hochreiter, S., Schmidhuber, J., 1997. Long short-term memory. *Neural Comput.* 9 (8), 1735–1780. <https://doi.org/10.1162/neco.1997.9.8.1735>.
- Hu, X., Waller, L.A., Al-Hamdan, M.Z., Crosson, W.L., Estes, M.G., Estes, S.M., Quattrocchi, D.A., Sarnat, J.A., Liu, Y., 2013. Estimating ground-level PM_{2.5} concentrations in the southeastern U.S. using geographically weighted regression. *Environ. Res.* 121, 1–10. <https://doi.org/10.1016/j.envres.2012.11.003>.
- Hu, X., Waller, L.A., Lyapustin, A., Wang, Y., Al-Hamdan, M.Z., Crosson, W.L., et al., 2014. Estimating ground-level PM_{2.5} concentrations in the Southeastern United States using MAIAC AOD retrievals and a two-stage model. *Remote Sens. Environ.* 140, 20–232. <https://doi.org/10.1016/j.rse.2013.08.032>.
- Huang, K., Xiao, Q., Meng, X., Geng, G., Wang, Y., Lyapustin, A., Gu, D., Liu, Y., 2018. Predicting monthly high-resolution PM_{2.5} concentrations with random forest model in the North China Plain. *Environ. Pollut.* 242, 675–683. <https://doi.org/10.1016/j.envpol.2018.07.016>.
- Jeong, C.H., Wang, J.M., Hilker, N., Debosz, J., Sofowote, U., Su, Y., Noble, M., Healy, R.M., Munoz, T., Dabek-Zlotorzynska, E., et al., 2019. Temporal and spatial variability of traffic-related PM_{2.5} sources: comparison of exhaust and non-exhaust emissions. *Atmos. Environ.* 198 (1), 55–69. <https://doi.org/10.1016/j.atmosenv.2018.10.038>.
- Kaufman, Y.J., Tanré, D., Remer, L.A., Vermote, E.F., Chu, A., Holben, B.N., 1997. Operational remote sensing of tropospheric aerosol over land from EOS moderate resolution imaging spectroradiometer. *J. Geophys. Res. Atmos.* 102 (D14) <https://doi.org/10.1029/96JD03988>, 17051–17067.
- Koelemeijer, R.B.A., Homan, C.D., Matthijsen, J., 2006. Comparison of spatial and temporal variations of aerosol optical thickness and particulate matter over Europe. *Atmos. Environ.* 40 (27), 5304–5315. <https://doi.org/10.1016/j.atmosenv.2006.04.044>.
- Lee, H.J., Liu, Y., Coull, B.A., Schwartz, J., Koutrakis, P., 2011. A novel calibration approach of MODIS AOD data to predict PM_{2.5} concentrations. *Atmos. Chem. Phys.* 11 (15), 7991–8002. <https://doi.org/10.5194/acp-11-7991-2011>.
- Leonardi, G.S., Houthuijs, D., Steerenberg, P.A., Fletcher, T., Armstrong, B., Antova, T., Lochman, I., Lochmanová, A., Rudnai, P., Erdei, E., et al., 2000. Immune biomarkers in relation to exposure to particulate matter: a cross-sectional survey in 17 cities of central Europe. *Inhal. Toxicol.* 12 (4), 1–14. <https://doi.org/10.1080/08958370050164833>.
- Li, T., Shen, H., Zeng, C., Yuan, Q., Zhang, L., 2017a. Point-surface fusion of station measurements and satellite observations for mapping PM_{2.5} distribution in China: methods and assessment. *Atmos. Environ.* 152, 477–489. <https://doi.org/10.1016/j.atmosenv.2017.01.004>.
- Li, T., Shen, H., Yuan, Q., Zhang, X., Zhang, L., 2017b. Estimating ground-level PM_{2.5} by fusing satellite and station observations: a geo-intelligent deep learning approach. *Geophys. Res. Lett.* 44 (23), 11985–11993. <https://doi.org/10.1002/2017gl075710>.
- Li, T., Shen, H., Yuan, Q., Zhang, L., 2020. Geographically and temporally weighted neural networks for satellite-based mapping of ground-level PM_{2.5}. *ISPRS J. Photogrammetry Remote Sens.* 167, 178–188. <https://doi.org/10.1016/j.isprsjprs.2020.06.019>.
- Li, Y., Chen, Q., Zhao, H., Wang, L., Tao, R., 2015. Variations in PM₁₀, PM_{2.5} and PM_{1.0} in an urban area of the Sichuan basin and their relation to meteorological factors. *Atmosphere* 6, 150–163. <https://doi.org/10.3390/atmos6010150>.
- Liu, F., Sun, F., Liu, W., Wang, T., Wang, H., Wang, X., Lim, W.H., 2019a. On wind speed pattern and energy potential in China. *Appl. Energy* 236, 867–876. <https://doi.org/10.1016/j.apenergy.2018.12.056>.
- Liu, J.J., Weng, F.Z., Li, Z.Q., 2019b. Satellite-based PM_{2.5} estimation directly from reflectance at the top of the atmosphere using a machine learning algorithm. *Atmos. Environ.* 208, 113–122. <https://doi.org/10.1016/j.atmosenv.2019.04.002>.
- Liu, R., Ma, Z., Liu, Y., Shao, Y., Zhao, W., Bi, J., 2020. Spatiotemporal distributions of surface ozone levels in China from 2005 to 2017: a machine learning approach. *Environ. Int.* 142, 105823 <https://doi.org/10.1016/j.envint.2020.105823>.
- Liu, Y., 2014. Monitoring PM_{2.5} from space for health: past, present, and future directions. *EMedia* 6, 6–10.
- Luo, J., Du, P., Samat, A., Xia, J., Che, M., Xue, Z., 2017. Spatiotemporal pattern of PM_{2.5} concentrations in mainland China and analysis of its influencing factors using geographically weighted regression. *Sci. Rep.* 7, 40607 <https://doi.org/10.1038/srep40607>.
- Ma, Z., Hu, X., Huang, L., Bi, J., Liu, Y., 2014. Estimating ground-level PM_{2.5} in China using satellite remote sensing. *Environ. Sci. Technol.* 48 (13), 7436–7444. <https://doi.org/10.1021/es5009399>.
- Pak, U., Ma, J., Ryu, U., Ryom, K., Juhyok, U., Pak, K., Pak, C., 2020. Deep learning-based PM_{2.5} prediction considering the spatiotemporal correlations: a case study of Beijing, China. *Sci. Total Environ.* 699, 133561 <https://doi.org/10.1016/j.scitotenv.2019.07.367>.
- Qin, D., Yu, J., Zou, G., Yong, R., Zhao, Q., Zhang, B., 2019. A novel combined prediction scheme based on CNN and LSTM for urban PM_{2.5} concentration. *IEEE Access* 7, 20050. <https://doi.org/10.1109/ACCESS.2019.2897028>.
- Qiu, H., Tian, L.W., Pun, V.C., Ho, K.F., Wong, T.W., Yu, I.T.S., 2014. Coarse particulate matter associated with increased risk of emergency hospital admissions for pneumonia in Hong Kong. *Thorax* 69, 1027–1033. <https://doi.org/10.1136/thoraxjnl-2014-205429>.
- Raaschou-Nielsen, O., Andersen, Z.J., Beelen, R., Samoli, E., Stafoggia, M., Weinmayr, G., Hoffmann, B., Fischer, P., Nieuwenhuijsen, M.J., Brunekreef, B., et al., 2013. Air pollution and lung cancer incidence in 17 European cohorts: prospective analyses from the European Study of Cohorts for Air Pollution Effects (ESCAPE). *Lancet Oncol.* 14 (9), 813–822. [https://doi.org/10.1016/s1470-2045\(13\)70279-1](https://doi.org/10.1016/s1470-2045(13)70279-1).
- Shen, H., Li, T., Yuan, Q., Zhang, L., 2018. Estimating regional ground-level PM_{2.5} directly from satellite top-of-atmosphere reflectance using deep belief networks. *J. Geophys. Res. Atmos.* 123 (24), 13875–13886. <https://doi.org/10.1029/2018jd028759>.
- Shin, M., Kang, Y., Park, S., Im, J., Yoo, C., Quackenbush, L.J., 2020. Estimating ground-level particulate matter concentrations using satellite-based data: a review. *Gisci. Remote Sens.* 57 (2), 174–189. <https://doi.org/10.1080/15481603.2019.1703288>.
- Srivastava, N., Hinton, G., Krizhevsky, A., Sutskever, I., Salakhutdinov, R., 2014. Dropout: a simple way to prevent neural networks from overfitting. *J. Mach. Learn. Res.* 15 (1), 1929–1958.
- Stafoggia, M., Bellander, T., Bucci, S., Davoli, M., de Hoogh, K., de Donato, F., Gariazzo, C., Lyapustin, A., Michelozzi, P., Renzi, M., et al., 2019. Estimation of daily PM₁₀ and PM_{2.5} concentrations in Italy, 2013–2015, using a spatiotemporal land-use random-forest model. *Environ. Int.* 124, 170–179. <https://doi.org/10.1016/j.envint.2019.01.016>.
- Song, Z., Fu, D., Zhang, X., Han, X., Song, J., Zhang, J., Wang, J., Xia, X., 2019. MODIS AOD sampling rate and its effect on PM_{2.5} estimation in North China. *Atmos. Environ.* 209, 14–22. <https://doi.org/10.1016/j.atmosenv.2019.04.020>.
- Tong, X., Sun, S., 2017. Long short-term memory network for wireless channel prediction. In: *Signal and Information Processing, Networking and Computers, ICSINC 2017. Lecture Notes in Electrical Engineering*, vol. 473. Springer, Singapore. https://doi.org/10.1007/978-981-10-7521-6_3.
- Tzaniis, C.G., Alimissis, A., Philippopoulos, K., Deligiorgi, D., 2019. Applying linear and nonlinear models for the estimation of particulate matter variability. *Environ. Pollut.* 246, 89–98. <https://doi.org/10.1016/j.envpol.2018.11.080>.
- Wang, W., Mao, F., Du, L., Pan, Z., Gong, W., Fang, S., 2017. Deriving hourly PM_{2.5} concentrations from himawari-8 AODs over Beijing–Tianjin–Hebei in China. *Rem. Sens.* 9 (8), 858. <https://doi.org/10.3390/rs9080858>.
- Wang, W., Zhang, W., Dong, S., Yonemachi, S., Lu, S., Wang, Q., 2020. Characterization, pollution sources, and health risk of ionic and elemental constituents in PM_{2.5} of wuhan, Central China. *Atmosphere* 11 (7), 760. <https://doi.org/10.3390/atmos11070760>.
- Wang, Y., Yuan, Q., Li, T., Shen, H., Zheng, L., Zhang, L., 2019. Large-scale MODIS AOD products recovery: spatial-temporal hybrid fusion considering aerosol variation mitigation. *ISPRS J. Photogrammetry Remote Sens.* 157, 1–12. <https://doi.org/10.1016/j.isprsjprs.2019.08.017>.
- Wei, J., Huang, W., Li, Z., Xue, W., Peng, Y., Sun, L., Cribb, M., 2019. Estimating 1-km-resolution PM_{2.5} concentrations across China using the space-time random forest approach. *Remote Sens. Environ.* 231, 111221 <https://doi.org/10.1016/j.rse.2019.111221>.
- Werner, M., Kryza, M., Pagowski, M., Guzowski, J., 2019. Assimilation of PM_{2.5} ground base observations to two chemical schemes in WRF-Chem – the results for the winter and summer period. *Atmos. Environ.* 200, 178–189. <https://doi.org/10.1016/j.atmosenv.2018.12.016>.
- Wu, Q., Lin, H., 2019. Daily urban air quality index forecasting based on variational mode decomposition, sample entropy and LSTM neural network. *Sustain. Cities Soc.* 50, 101657 <https://doi.org/10.1016/j.scs.2019.101657>.
- Xie, Y., Wang, Y., Zhang, K., Dong, W., Lv, B., Bai, Y., 2015. Daily estimation of ground-level PM_{2.5} concentrations over Beijing using 3 km resolution MODIS AOD. *Environ. Sci. Technol.* 49 (20), 12280–12288. <https://doi.org/10.1021/acs.est.5b01413>.
- Xue, Y., Li, Y., Guang, J., Tugui, A., She, L., Qin, K., Fan, C., Che, Y., Xie, Y., Wen, Y., Wang, Z., 2020. Hourly PM_{2.5} estimation over central and eastern China based on himawari-8 data. *Rem. Sens.* 12, 855. <https://doi.org/10.3390/rs12050855>.
- Yan, X., Liang, C., Jiang, Y., Luo, N., Zang, Z., Li, Z., 2020a. A deep learning approach to improve the retrieval of temperature and humidity profiles from a ground-based microwave radiometer. *IEEE Trans. Geosci. Rem. Sens.* <https://doi.org/10.1109/TGRS.2020.2987896>.
- Yan, X., Zang, Z., Luo, N., Jiang, Y., Li, Z., 2020b. New interpretable deep learning model to monitor real-time PM_{2.5} concentrations from satellite data. *Environ. Int.* 144, 106060 <https://doi.org/10.1016/j.envint.2020.106060>.
- Yang, Q., Yuan, Q., Li, T., Shen, H., Zhang, L., 2017. The relationships between PM_{2.5} and meteorological factors in China: seasonal and regional variations. *Int. J. Environ. Res. Publ. Health* 14 (12), 1510. <https://doi.org/10.3390/ijerph14121510>.
- Yang, W., Deng, M., Xu, F., Wang, H., 2018. Prediction of hourly PM_{2.5} using a space-time support vector regression model. *Atmos. Environ.* 181, 12–19. <https://doi.org/10.1016/j.atmosenv.2018.03.015>.
- Yao, F., Wu, J., Li, W., Peng, J., 2019. A spatially structured adaptive two-stage model for retrieving ground-level PM_{2.5} concentrations from VIIRS AOD in China. *ISPRS J. Photogrammetry Remote Sens.* 151, 263–276. <https://doi.org/10.1016/j.isprsjprs.2019.03.011>.

- You, W., Zang, Z., Zhang, L., Li, Y., Pan, X., Wang, W., 2016. National-scale estimates of ground-level PM_{2.5} concentration in China using geographically weighted regression based on 3 km resolution MODIS AOD. *Rem. Sens.* 8 (3), 184. <https://doi.org/10.3390/rs8030184>.
- Zang, L., Mao, F., Guo, J., Gong, W., Wang, W., Pan, Z., 2018. Estimating hourly PM₁ concentrations from Himawari-8 aerosol optical depth in China. *Environ. Pollut.* 241, 654–663. <https://doi.org/10.1016/j.envpol.2018.05.100>.
- Zeng, Q., Chen, L., Zhu, H., Wang, Z., Wang, X., Zhang, L., Gu, T., Zhu, G., Zhang, Y., 2018. Satellite-based estimation of hourly PM_{2.5} concentrations using a vertical-humidity correction method from himawari-AOD in hebei. *Sensors* 18, 3456. <https://doi.org/10.3390/s18103456>.
- Zhang, B., Zhang, H., Zhao, G., Lian, J., 2020. Constructing a PM_{2.5} concentration prediction model by combining auto-encoder with Bi-LSTM neural networks. *Environ. Model. Software* 124, 104600. <https://doi.org/10.1016/j.envsoft.2019.104600>.